Chemical Science

ROYAL SOCIETY OF CHEMISTRY

EDGE ARTICLE

View Article Online
View Journal | View Issue

Cite this: *Chem. Sci.*, 2024, **15**, 1820

All publication charges for this article have been paid for by the Royal Society of Chemistry

Received 11th October 2023
Accepted 22nd December 2023

DOI: 10.1039/d3sc05451a

rsc.li/chemical-science

Triazenide-supported [Cu_4S] structural mimics of Cu_Z that mediate N_2O disproportionation rather than reduction†

Neal P. Mankad *

As part of the nitrogen cycle, environmental nitrous oxide (N_2O) undergoes the N_2O reduction reaction (N_2ORR) catalyzed by nitrous oxide reductase, a metalloenzyme whose catalytic active site is a tetranuclear copper–sulfide cluster (Cu_Z). On the other hand, heterogeneous Cu catalysts on oxide supports are known to mediate decomposition of N_2O (deN_2O) by disproportionation. In this study, a Cu_Z model system supported by triazenide ligands is characterized by X-ray crystallography, NMR and EPR spectroscopies, and electronic structure calculations. Although the triazenide-ligated $Cu_4(\mu_4\text{-}S)$ clusters are closely related to previous formamidinate derivatives, which differ only in replacement of a remote N atom for a CH group, divergent reactivity with N_2O is observed. Whereas the formamidinate-ligated clusters were previously shown to mediate single-turnover N_2ORR, the triazenide-ligated clusters are found to mediate deN_2O, behavior that was previously unknown to natural or synthetic copper–sulfide clusters. The reaction pathway for deN_2O by this model system, including previously unidentified transition state models for N_2O activation in N–O cleavage and O–O coupling steps, are included. The divergent reactivity of these two related but subtly different systems point to key factors influencing behavior of Cu-based catalysts for N_2ORR (*i.e.*, Cu_Z) and deN_2O (*e.g.*, CuO/CeO_2).

Introduction

Anthropogenic nitrous oxide (N_2O) emissions have approximately 500 times the global warming potential of CO_2 per molecule[1] and represent the leading cause of ozone layer depletion.[2] Therefore, it is critical to understand the mechanisms by which both natural and synthetic catalysts convert N_2O to benign compounds.[3–5] In nature, N_2O is converted to N_2 according to eqn (1) as part of the nitrogen cycle.[6,7] This N_2O reduction reaction (N_2ORR) is catalyzed by nitrous oxide reductase (N_2OR),[8–10] a copper-dependent enzyme crucial to bacterial denitrification. The catalytic site of N_2OR is a copper–sulfide cluster known as Cu_Z,[11] which has consistently been found to contain a $[Cu_4(\mu_4\text{-}S)]^{n+}$ core in all its catalytically active forms.[12–15] Alternatively, heterogeneous catalysts are known to mediate the decomposition of N_2O (deN_2O) according to eqn (2). Although this disproportionation reaction is catalyzed most efficiently by Rh,[16] explorations of earth-abundant alternatives have identified Cu-doped zeolites and CuO/CeO_2 as viable catalyst materials.[17–19]

$$N_2O + 2H^+ + 2e^- \rightarrow N_2 + H_2O \quad (1)$$

$$N_2O \rightarrow N_2 + \tfrac{1}{2}O_2 \quad (2)$$

Our group has reported previous synthetic studies on structural[20–22] and functional[23–25] mimics of Cu_Z involving $[Cu_4(\mu_4\text{-}S)]$ cores supported by bridging diphosphine or formamidinate ligands.[11] One of these complexes, $[Cu_4(\mu_4\text{-}S)(NCN)_4]^-$ ($[\mathbf{1}^{\mathbf{C}}]^-$), not only possesses an electronic structure similar to Cu_Z according to XAS analysis[24] but also was found to mediate a single turnover of N_2ORR, producing N_2 and O^{2-} along with $[Cu_4(\mu_4\text{-}S)(NCN)_4]$ ($\mathbf{1}^{\mathbf{C}}$) quantitatively (NCN = [MesN = CH-NMes]$^-$, see Scheme 1).[23] In this reaction, it was proposed that one equivalent of $[\mathbf{1}^{\mathbf{C}}]^-$ activates the N_2O substrate (mimicking Cu_Z in N_2OR) while another $[\mathbf{1}^{\mathbf{C}}]^-$ equivalent acts as a sacrificial electron donor (mimicking the Cu_A electron

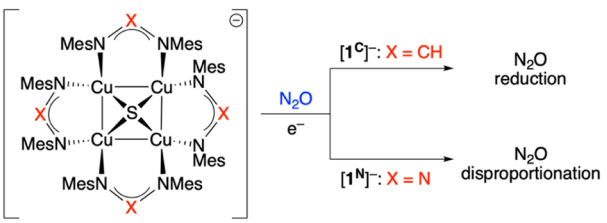

Scheme 1 Divergent N_2O reactivity of Cu_4S model systems (Mes = 2,4,6-$Me_3C_6H_2$).

Department of Chemistry, University of Illinois Chicago, Chicago, IL 60607, USA. E-mail: npm@uic.edu

† Electronic supplementary information (ESI) available: Experimental section and spectra data, crystallographic data, computational output. CCDC 2299540 2299541. For ESI and crystallographic data in CIF or other electronic format see DOI: https://doi.org/10.1039/d3sc05451a

transfer site in N_2OR). Based on computational modeling, μ-1,3-N_2O binding across a Cu–S edge of the cluster enabled by sulfide redox non-innocence was proposed,[24] although details of the N–O bond breaking pathway (*e.g.*, the transition state structure) were not elucidated. This manuscript details the synthesis, characterization, and N_2O reactivity of an analogous $[Cu_4(\mu_4\text{-}S)(NNN)]^{n-}$ system (NNN = $[MesN{=}N\text{-}NMes]^-$; n = 0, 1; see Scheme 1). Unlike its formamidinate analogue $[\mathbf{1^C}]^-$, the triazenide derivative $[\mathbf{1^N}]^-$ reacts with N_2O in a 1 : 1 stoichiometry upon reductive activation, mediating a single turnover of deN_2O rather than N_2ORR. Computational analysis of the deN_2O process includes transition state models for N–O cleavage and O–O coupling steps that were not identified in previous studies. The divergent selectivity of N_2ORR for $[\mathbf{1^C}]^-$ *vs.* deN_2O for $[\mathbf{1^N}]^-$ points to key factors influencing behavior of Cu-based catalysts for N_2ORR (*i.e.*, Cu_Z) and deN_2O (*e.g.*, CuO/CeO_2).

Results and discussion

Synthesis and characterization of the $\mathbf{1^N}$ system somewhat parallel those of the $\mathbf{1^C}$ system[21–24] but will be detailed here to facilitate important comparisons between complexes that are summarized in Table 1.

Addition of a toluene solution of elemental sulfur to a bright yellow THF solution of dicopper(I) precursor, $Cu_2(NNN)_2$, immediately produced an inky blue solution from which $[Cu_4(\mu_4\text{-}S)(NNN)_4]$ ($\mathbf{1^N}$) began to spontaneously crystallize. Complex $\mathbf{1^N}$ is highly crystalline, showing only sparing solubility in THF, CH_2Cl_2, and $CHCl_3$ and no measurable solubility in CH_3CN, Et_2O, and toluene. Notably, $\mathbf{1^N}$ is indefinitely stable on a benchtop in open air. The ^{1}H NMR of $\mathbf{1^N}$ in $CDCl_3$ (Fig. S1†) is consistent with two inequivalent NNN environments (*syn* and *anti* to the μ_4-S ligand, respectively), each with restricted N–C bond rotation. A similar interpretation of the ^{1}H NMR spectrum of $\mathbf{1^C}$ was attributed to intramolecular π-stacking interactions between neighboring mesityl groups evident by X-ray crystallography.[23] The UV-Vis-NIR spectrum of $\mathbf{1^N}$ in CH_2Cl_2 (Fig. 1a) is dominated by an intense charge transfer transition at λ_{max} = 602 nm ($\varepsilon = 1.2 \times 10^4$ M^{-1} cm^{-1}) with a shoulder at $\lambda_{max} \approx$ 768 nm. Another feature at higher energy (λ_{max} = 369 nm) is likely ligand-based, as it appears in all complexes examined, including previously reported $Cu_2(NNN)_2$.[26] For comparison, the analogous charge transfer transitions for $\mathbf{1^C}$, which is purple-colored, were observed at 561 ($\varepsilon = 1.4 \times 10^4$ M^{-1} cm^{-1}) and ~470 nm (shoulder).[22]

Complex $\mathbf{1^N}$ crystallized with cubic symmetry in the $R\bar{4}3n$ space group, with the molecule residing on a crystallographic special position. The asymmetric unit (Fig. S3†) contains a single NNN ligand, a single Cu atom disordered over two positions, and a single S atom. Applying crystallographic symmetry elements reveals a cluster with four well-ordered NNN ligands related by a molecular S_4 axis, along with a disordered inorganic core with eight distinct Cu positions and two S positions (Fig. S3†). To assist with interpretation, a computational model of $\mathbf{1^N}$ was built and optimized by DFT. (Here and throughout the study, computational models use methyl groups in place of mesityls.) The resulting structure (Fig. 1b) features a rectangle-based pyramidal Cu_4S core with Cu–Cu distances of 2.45 and 2.85 Å and Cu–S distances of 2.24 Å. The crystallographic model was then analyzed by grouping together four Cu atoms with one S position and the other four Cu atoms with the other S position to match the computational model as closely as possible. This analysis indicated a rectangular pyramidal Cu_4S core disordered over two positions, with experimental Cu–Cu distances of 2.405(3) and 2.965(3) Å and Cu–S distances of 2.176(2) Å (Fig. 1a). Grouping together the Cu and S atoms in alternative ways provided geometries dissimilar to the computational model, *e.g.*, with unreasonably long Cu–S bonds. Additionally, this interpretation of the crystallographic data provides a model that is isostructural to $\mathbf{1^C}$, which was reported to have Cu–Cu distances of 2.4226(6) and 3.0353(6) Å within its rectangle-based pyramidal Cu_4S core.[22]

The cyclic voltammogram of $\mathbf{1^N}$ in ^{n}Bu$_4$NPF$_6$/THF (Fig. S6†) showed a reversible reduction at −0.85 V *vs.* $FeCp_2^{+/0}$ to the $[\mathbf{1^N}]^-$ state, and an irreversible reduction at lower potentials to the $[\mathbf{1^N}]^{2-}$ state that is unstable on this timescale. The redox behavior mirrors that of $\mathbf{1^C}$, which possesses a reversible reduction at −1.28 V and an irreversible reduction at lower potentials.[22] Thus, the substitution of four formamidinate

Table 1 Data comparison of triazenide- and formamidinate-ligated Cu_4S clusters

Property	$Cu_4S(NNN)_4$ ($\mathbf{1^N}$)	$[Cu_4S(NNN)_4]^-$ ($[\mathbf{1^N}]^-$)	$Cu_4S(NCN)_4$ ($\mathbf{1^C}$)[a]	$[Cu_4S(NCN)_4]^-$ ($[\mathbf{1^C}]^-$)[b]
λ_{max} (nm)	602, 768 (sh)	620, 934	470 (sh), 561	566
ε (M^{-1} cm^{-1})	1.2×10^4	4.1×10^3, 3.3×10^3	1.4×10^4	8.6×10^3
d (Cu···Cu) (Å)	2.405(3)	2.5853(16)	2.4226(6)	2.502(1)
	2.965(3)	2.6031(16)	3.0353(6)	2.809(1)
	2.405(3)[c]	2.5853(16)[c]	2.4226(6)[c]	2.532(1)
	2.965(3)[c]	2.6031(16)[c]	3.0353(6)[c]	2.831(2)
$E°$ (V *vs.* $[FeCp_2]^{+/0}$)	−0.85	irreversible	−1.28	irreversible
g tensors	n/a	2.143, 2.066, 2.005 (rhombic)	n/a	2.043, 2.090 (axial)
$A(^{63,65}Cu)$ tensors (MHz)	n/a	≤122, 90, 100 (from H-strain)	n/a	15, 100
Redox-active MO[d]	S 3p, 25%	S 3p, 26%	S 3p, 21%	S 3p, 20%
	Cu 3d, 11% each	Cu 3d, 12% each	Cu 3d, 13% each	Cu 3d, 14% each

[a] From Johnson *et al.*;[22] [b] From Johnson *et al.*[23] and Rathnayaka *et al.*;[24] [c] Generated by crystallography symmetry. [d] Mulliken populations for the LUMO and SOMO, respectively.

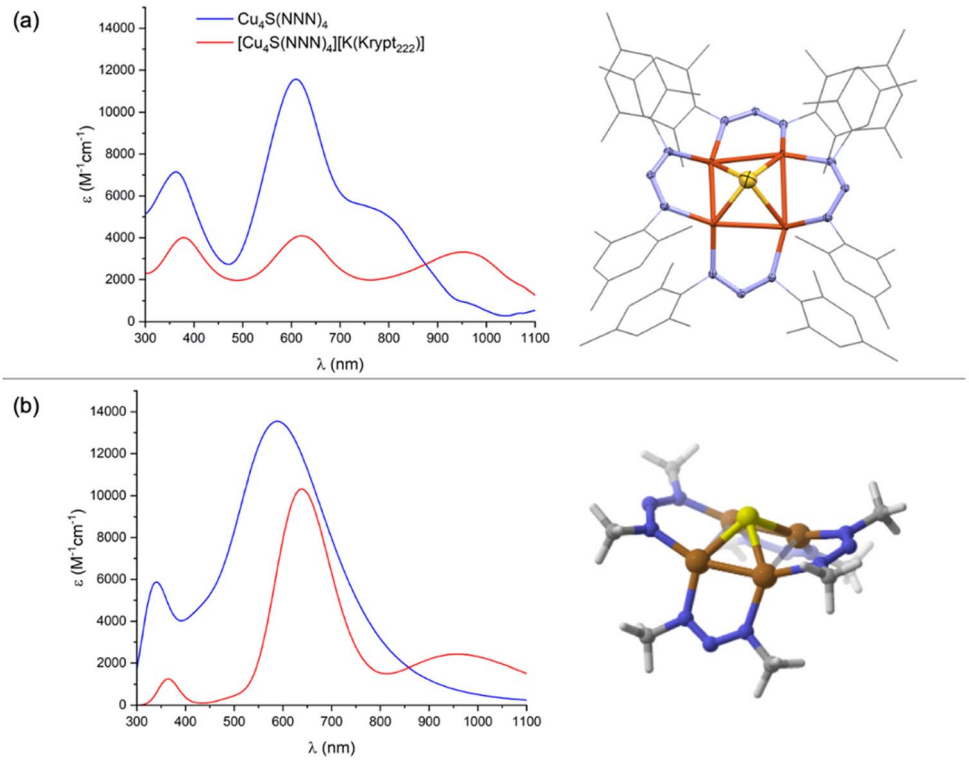

Fig. 1 (a) Experimental and (b) computational data: UV-Vis-NIR of neutral (blue, CH_2Cl_2) and anionic (red, THF) forms of $\mathbf{1^N}$ (left) and molecular structures of the neutral redox state of $\mathbf{1^N}$ (right). The X-ray crystal structure is depicted as 50%-probability ellipsoids for non-C, H atoms and as wireframe for C atoms; H atoms are omitted; and only one component of the disordered Cu_4S core is shown. Computations were done at the B3LYP/def2TZVPP level of DFT using the CPCM implicit solvation model (CH_2Cl_2); computed UV-Vis-NIR spectra were generated using excitations calculated by TD-DFT and assuming 0.333 eV half-width at half height.

ligands for four triazenides shifts the redox potentials positively by approximately 0.4 V.

Chemical reduction of $\mathbf{1^N}$ was carried out with either $CoCp_2$ ($E^{o\prime} = -1.33$ V *vs.* $FeCp_2^{+/0}$) or $K[FeCp(CO)_2]$ ($E^{o\prime} = -1.8$ V *vs.* $FeCp_2^{+/0}$) in THF or CH_2Cl_2.[27] In each case, a subtle color change from inky blue to a duller blue was observed. While the $[\mathbf{1^N}][CoCp_2]$ salt was too insoluble for solution analysis, use of Kryptofix-222 to form $[\mathbf{1^N}][K(Krypt_{222})]$ provided material suitable for characterization. As expected, only resonances for the cationic portion were observed by ^{1}H NMR (Fig. S7†) due to the $S = 1/2$ ground state of the $[\mathbf{1^N}]^-$ anion. The $[\mathbf{1^N}][K(Krypt_{222})]$ salt is air-sensitive in solution, gradually converting to neutral $\mathbf{1^N}$ when left on the benchtop. The UV-Vis-NIR spectrum of $[\mathbf{1^N}][K(Krypt_{222})]$ in THF (Fig. 1a) has three main features, all of which have lower molar extinction coefficients than for corresponding peaks for $\mathbf{1^N}$. Charge transfer transitions at $\lambda_{max} =$ 382 nm and $\lambda_{max} = 620$ nm ($\varepsilon = 4.1 \times 10^3$ M^{-1} cm^{-1}) are minimally shifted in wavelength compared to $\mathbf{1^N}$. However, the feature for $\mathbf{1^N}$ at $\lambda_{max} = 768$ nm shifts significantly to $\lambda_{max} =$ 934 nm ($\varepsilon = 3.3 \times 10^3$ M^{-1} cm^{-1}) for $[\mathbf{1^N}]^-$. For comparison, purple-colored $[\mathbf{1^C}]^-$ was reported to have a charge transfer band at $\lambda_{max} = 566$ nm ($\varepsilon = 8.6 \times 10^3$ M^{-1} cm^{-1}), and no NIR data was reported in the previous study.[23] Generally, both $\mathbf{1^N}$ and $[\mathbf{1^N}]^-$ have their optical transitions shifted to longer wavelengths by 40–50 nm compared to $\mathbf{1^C}$ and $[\mathbf{1^C}]^-$.

Crystallization of $[\mathbf{1^N}][K(Krypt_{222})]$ invariably gave thin plates with very weak X-ray diffraction, and X-ray quality crystals of other salts of $[\mathbf{1^N}]^-$ (*e.g.*, $[\mathbf{1^N}][CoCp_2]$, $[\mathbf{1^N}][K(18\text{-crown-6})]$) were not obtained after repeated attempts. Compound $[\mathbf{1^N}][K(Krypt_{222})]$ crystallizes with orthorhombic symmetry in the $C222_1$ space group, with both cation and anion portions residing on crystallographic special positions (Fig. S9†). The $[K(Krypt_{222})]^+$ unit exhibited severe disorder. Furthermore, within the $[\mathbf{1^N}]^-$ unit, the S atom was disordered over two positions and the NNN ligands exhibited significant disorder, too. Fortunately, the four Cu positions were well ordered. The crystallographic data indicates that, upon reduction from $\mathbf{1^N}$ to $[\mathbf{1^N}]^-$, the Cu_4S core converts from a rectangular towards a square-based pyramid shape, with experimental Cu–Cu distances of 2.5853(16) and 2.6031(16) Å. A DFT model of $[\mathbf{1^N}]^-$ (Fig. S10†) was found to have computed Cu–Cu distances of 2.54 and 2.74 Å, which are also shifted from rectangular towards square shaped compared to the DFT model of $\mathbf{1^N}$ (*vide supra*). The change from rectangular to square shape in the Cu_4 base was also observed previously upon reduction of $\mathbf{1^C}$ to $[\mathbf{1^C}]^-$, the latter of which has experimental Cu–Cu distances of 2.502(1) and 2.809(1) Å.[23]

Having optimized computational models for $\mathbf{1^N}$ and $[\mathbf{1^N}]^-$, next we conducted TD-DFT calculations to better understand the electronic transitions evident by UV-Vis-NIR. As shown in Fig. 1b, the salient features of the experimental UV-Vis-NIR

spectra are well captured in the computed spectra, especially when considering that the computational models used a truncated [MeN═N–NMe]$^-$ ligand in place of the [MesN═N-NMes]$^-$ ligand used experimentally. For [$\mathbf{1}^{\mathbf{N}}$]$^-$, excitations calculated at 639 nm (experimental: 620 nm) and 961 nm (experimental: 934 nm) are both charge transfers into the LUMO (MO145β), which is a highly delocalized MO with 26% S 3p character, 48% Cu 3d character (12% per Cu), and significant contribution from the two NNN ligands *syn* to the μ_4-S atom (Fig. 2a). The transition calculated at 639 nm involves excitation of an electron from MO144β, which has 74% Cu 3d character. Thus, this transition can be viewed as a combination of Cu → S and Cu → NNN MLCT. The transition calculated at 961 nm involves excitation of an electron from MO141β, which is exclusively based on the four NNN ligands (<5% Cu 3d, <5% S 3p). Thus, this transition can be viewed as NNN → [Cu_4S] CT. The corresponding transitions for neutral $\mathbf{1}^{\mathbf{N}}$ are qualitatively similar but less readily interpreted because of some admixture of states *via* configuration interactions at each excitation wavelength (Fig. S4†).

The X-band EPR spectrum of [$\mathbf{1}^{\mathbf{N}}$][K($Krypt_{222}$)] at 77 K in a frozen CH_3CN/CH_2Cl_2 glass is shown in Fig. 2b. Fine structure was not well resolved in the first-derivative spectrum but was emphasized by plotting the second derivative (Fig. 2c). Surprisingly, hyperfine splitting due to the four ^{63,65}Cu nuclei (I_{Cu} = 3/2) was not evident. Instead, the spectra were best simulated with hyperfine splitting from two equivalent ^{14}N nuclei. The simulation also required inclusion of significant "*H*-strain", *i.e.*, unresolved hyperfine coupling that can be assigned to a combination of the four ^{63,65}Cu centers and remaining ^{14}N nuclei. This pattern can be rationalized by analyzing the spin density from the DFT model of [$\mathbf{1}^{\mathbf{N}}$]$^-$, which is plotted in Fig. 2d. Of the total 1e$^-$ spin, only 0.113e$^-$ resides on each Cu center (0.452e$^-$ total), meaning that most of the unpaired spin is ligand-centered. The largest contributor is the μ_4-S atom, which carries 0.300e$^-$. Of the remaining 0.248e$^-$ of NNN-centered spin, nearly all resides on the two NNN ligands *syn* to the μ_4-S ligand, with effectively none on the two *anti*-NNN ligands. Thus, the $A(^{14}N)$ coupling observed by EPR spectroscopy can be assigned to the central N-atoms of the two *syn*-NNN ligands. The small and apparently unresolved $A(^{63,65}Cu)$ coupling is consistent with the high degree of covalency (*i.e.*, μ_4-S and NNN redox non-innocence) apparent from calculations. Although the EPR spectroscopy of [$\mathbf{1}^{\mathbf{C}}$]$^-$ differs in that it is an axial signal dominated by $A(^{63,65}Cu)$ coupling,[23] nonetheless the redox-active MOs for both the $\mathbf{1}^{\mathbf{N}}$ and $\mathbf{1}^{\mathbf{C}}$ systems are similar to each other (Table 1).[24]

No reaction was observed when [$\mathbf{1}^{\mathbf{N}}$][K($Krypt_{222}$)] was exposed to N_2O (1 atm) in CH_2Cl_2. This behavior contrasts that of [$\mathbf{1}^{\mathbf{C}}$][K(18-crown-6)], which converts quantitatively to $\mathbf{1}^{\mathbf{C}}$ under the same conditions.[23] In the latter case, it was proposed that reversible N_2O binding to [$\mathbf{1}^{\mathbf{C}}$][K(18-crown-6)] to transiently form [$\mathbf{1}^{\mathbf{C}}\cdot N_2O$][K(18-crown-6)] shifts the reduction potential such that a second equivalent of [$\mathbf{1}^{\mathbf{C}}$][K(18-crown-6)] can act as an electron donor, producing [$\mathbf{1}^{\mathbf{C}}\cdot N_2O$][K(18-crown-6)]$_2$ and $\mathbf{1}^{\mathbf{C}}$ (*i.e.*, N_2O-induced disproportionation of the copper cluster). The shift of the $\mathbf{1}^{\mathbf{N}}$/[$\mathbf{1}^{\mathbf{N}}$]$^-$ potential to more positive values

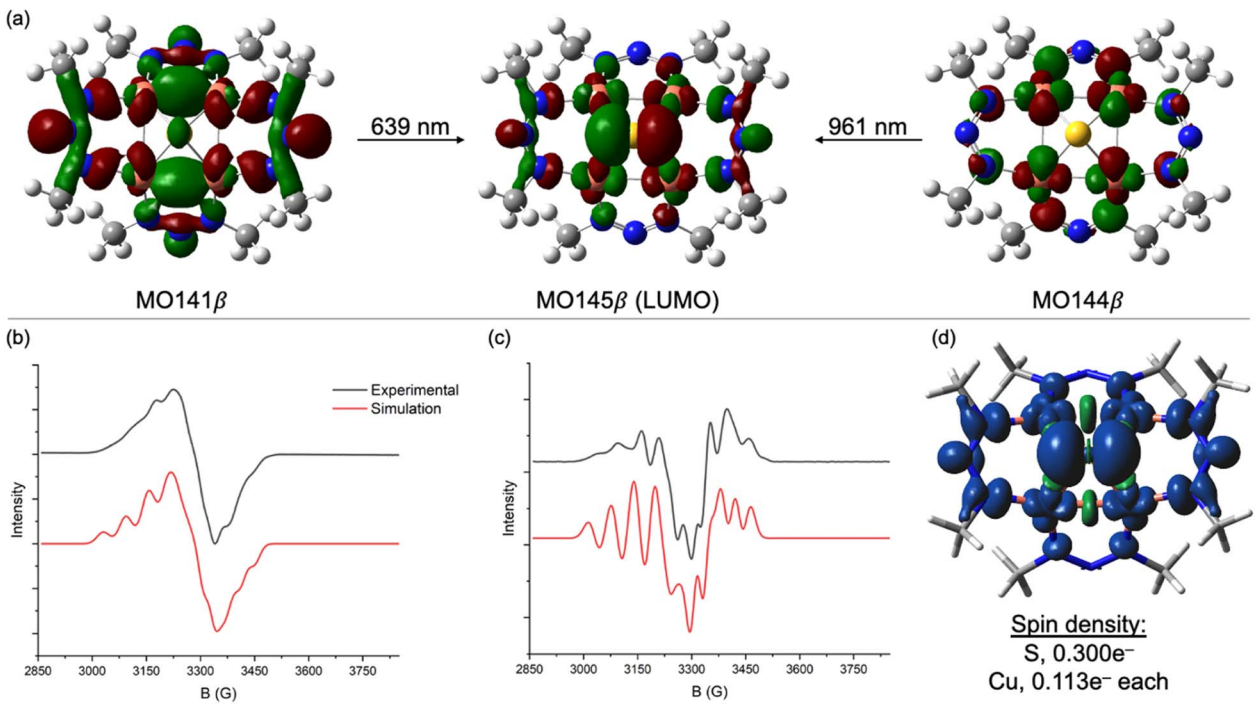

Fig. 2 (a) Charge transfer transitions (0.03 isosurfaces) for [$\mathbf{1}^{\mathbf{N}}$]$^-$ calculated by TD-DFT at the B3LYP/def2TZVPP level using the CPCM implicit solvation model (CH_2Cl_2). Experimental and simulated X-band EPR spectroscopy for [$\mathbf{1}^{\mathbf{N}}$][K($Krypt_{222}$)] in frozen CH_3CN/CH_2Cl_2 (1 : 1) glass at 77 K: (b) 1st derivative and (c) 2nd derivative spectra. (d) Spin density (0.001 isosurface) for [$\mathbf{1}^{\mathbf{N}}$]$^-$ calculated by DFT. EPR simulation parameters: g = 2.143, 2.066, 2.005; A = 193, 68, 98 MHz for 2 equivalent ^{14}N nuclei; *H*-strain = 122, 90, 100 MHz; Gaussian line broadening = 0.43.

apparently prevents such N_2O-induced disproportionation from occurring spontaneously for the triazenide derivative. Therefore, the reaction was repeated with a stronger sacrificial electron donor, $CoCp_2$, to reduce a transiently-formed $[\mathbf{1}^{\mathbf{N}}\cdot N_2O][K(Krypt_{222})]$. A 1 : 1 mixture of $[\mathbf{1}^{\mathbf{N}}][K(Krypt_{222})]$ and $CoCp_2$ in CH_2Cl_2 solution was observed to darken slightly upon exposure to N_2O (1 atm). Over 24 h, the major species in solution remained $[\mathbf{1}^{\mathbf{N}}]^-$ according to UV-Vis-NIR spectroscopy. However, analysis of the reaction mixture by ^{1}H NMR spectroscopy indicated small conversion (~10%) of $CoCp_2$ to $[CoCp_2]^+$ along with formation of a new, diamagnetic product (**2**) containing the NNN ligand. The same product **2** was generated when exposing a 1 : 2 mixture of $\mathbf{1}^{\mathbf{N}}$ and $CoCp_2$ to N_2O (1 atm) or when replacing N_2O with excess Me_3NO under N_2. Compound **2** could be extracted into toluene or Et_2O, which served to separate it from $[CoCp_2]^+$, $[\mathbf{1}^{\mathbf{N}}]^-$, and/or $\mathbf{1}^{\mathbf{N}}$. Washing **2** with pentane served to separate it from $CoCp_2$ (and excess Me_3NO where relevant, see Fig. S12†). At this point, compound **2** was found to have a brown color, with a UV-Vis-NIR spectrum in CH_2Cl_2 (Fig. 3a) showing a single distinct feature at $\lambda_{max} = 420$ nm but lacking any well-defined charge transfer transitions in the 600–1000 nm region as observed for $\mathbf{1}^{\mathbf{N}}$ and $[\mathbf{1}^{\mathbf{N}}]^-$. From these collected observations, it can be concluded that (1) the reaction involves O-atom transfer from N_2O since Me_3NO can replace it, (2) the resulting product **2** is diamagnetic and neutral in charge based on NMR characterization and solubility properties, and (3) compound **2** likely lacks the μ_4-S atom that would produce low-energy CT electronic transitions.

Unfortunately, all reaction conditions explored consistently provided only low conversion (<15%) to **2**, with the remaining mass balance being predominantly $[\mathbf{1}^{\mathbf{N}}]^-$. Furthermore, repeated attempts at obtaining X-ray quality crystals of **2** failed. The identity of **2** was made clear by analyzing it using EI-HRMS. The parent ion mass and isotope distribution (Fig. 3a) indicate the empirical formula, $Cu_4(O_2)(NNN)_4$. To investigate this possibility further, the structure of **2** assuming that formula was modeled computationally. Two energy minima were located: one with μ_2:η^2 binding of an O_2 unit to one Cu from the periphery of the Cu_4 core, and another with μ_3:η^2,η^1,η^1 binding of the O_2 unit to three Cu atoms in the capping position typically occupied by sulfide (Fig. S13†). The former isomer (Fig. 3b) was calculated to be lower in Gibbs free energy by -13.6 kcal mol^{-1}. The predicted UV-Vis-NIR spectrum (Fig. 3b) of this structure reproduces key features of the experimental spectrum, with a prominent absorbance at $\lambda_{max} = 448$ nm (experimental: 420 nm) that tails into the lower energy region of the spectrum without well-defined absorbance features in the 600–1000 nm region. The local structure within **2** of the $Cu(O_2)$ unit in a nitrogen-rich environment resembles 1 : 1 $Cu : O_2$ species that have been long studied since seminal works of Kitajima, Tolman, and others.[28,29] Notably, the presence of an absorbance at ~400 nm is characteristic of such compounds

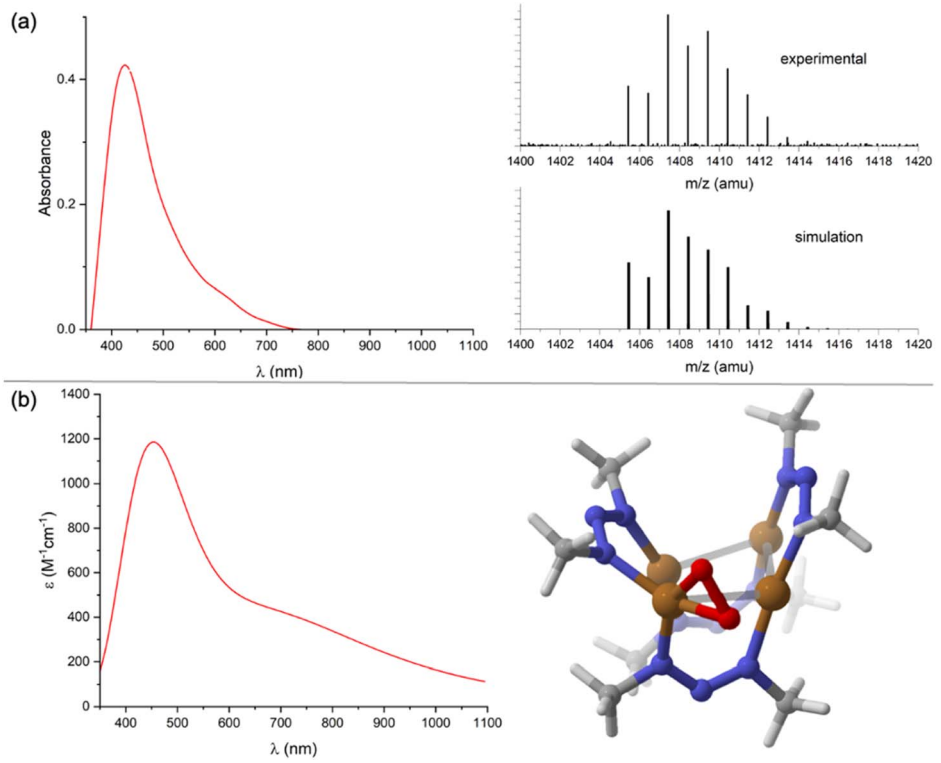

Fig. 3 Characterization of complex **2**: (a) experimental UV-Vis-NIR (left, CH_2Cl_2) and high-resolution mass spectrometry (right, positive EI mode) data; (b) computed UV-Vis-NIR spectrum (left) and molecular structure (right). Computations were done at the B3LYP/def2TZVPP level of DFT using the CPCM implicit solvation model (CH_2Cl_2); computed UV-Vis-NIR spectra were generated using excitations calculated by TD-DFT and assuming 0.45 eV half-width at half height.

and is typically assigned to the $\pi \rightarrow \pi^*$ transition of the bound O_2.[30] The calculated O–O distance of 1.37 Å in **2** and the short calculated Cu–O distances of 1.85 and 1.86 Å are all indicative of a highly reduced O_2 unit.[31,32] Curiously, the ^{1}H NMR spectrum for **2** shown only one set of NNN peaks, rather than the three sets expected based on the calculated structure. This is likely indicative of fluxionality due to the O_2 ligand rapidly hopping from Cu site to Cu site.

Based on these observations, a plausible mechanism for a hypothetical deN$_2$O reaction for is presented in Scheme 2. Reversible binding of N_2O to $[\mathbf{1^N}]^-$ would generate a small equilibrium concentration of $[\mathbf{1^N}\cdot N_2O]^-$. Despite $CoCp_2$ not being a strong enough reductant to spontaneously reduce $[\mathbf{1^N}]^-$, reduction of $[\mathbf{1^N}\cdot N_2O]^-$ could be spontaneous due to the π-accepting nature of N_2O raising the reduction potential of the Cu_4S core. The resulting $[\mathbf{1^N}\cdot N_2O]^{2-}$ intermediate would, then, be the active catalyst in the "fully reduced" 4Cu^{I} redox state.[33] Based on previous computational modeling with $[\mathbf{1^C}\cdot N_2O]^-$,[24] a μ-1,3-N_2O binding mode spanning a Cu–S cluster edge is proposed. Low conversion to **2** observed experimentally is likely due to inefficiency of this reductive activation process, *i.e.*, most of the dissolved complex remains unactivated as $[\mathbf{1^N}]^-$.

On the active cycle, loss of N_2 from $[\mathbf{1^N}\cdot N_2O]^{2-}$ would generate $[\mathbf{1^N}\cdot O]^{2-}$, which is proposed to feature μ_2-O^{2-} binding based on previous modeling for $[\mathbf{1^C}\cdot O]^{2-}$.[23] For N_2ORR chemistry associated with the $\mathbf{1^C}$ system, dissociation of O^{2-} from $[\mathbf{1^C}\cdot O]^{2-}$ generates $\mathbf{1^C}$, which can hypothetically undergo 2e$^-$ reduction under N_2O to regenerate $[\mathbf{1^C}\cdot N_2O]^{2-}$. In the $\mathbf{1^N}$ system, N_2ORR chemistry is not observed. Instead, a second N_2O molecule presumably intercepts $[\mathbf{1^N}\cdot O]^{2-}$ to generate $[\mathbf{1^N}\cdot O_2]^{2-}$ with loss of N_2. To complete the hypothetical deN$_2$O cycle, O_2 loss would form $[\mathbf{1^N}]^{2-}$, which would regenerate $[\mathbf{1^N}\cdot N_2O]^{2-}$ upon N_2O coordination. On the other hand, if S^{2-} dissociation outcompetes O_2 dissociation, then off-cycle species **2** is formed. (Other pathways to **2** cannot be ruled out, *vide infra*.) Experimentally, examination of the headspace gas above the N_2O reaction revealed only trace quantities of N_2 and O_2, consistent with the off-cycle decomposition to **2** outcompeting on-cycle N_2O-for-O_2 substitution.

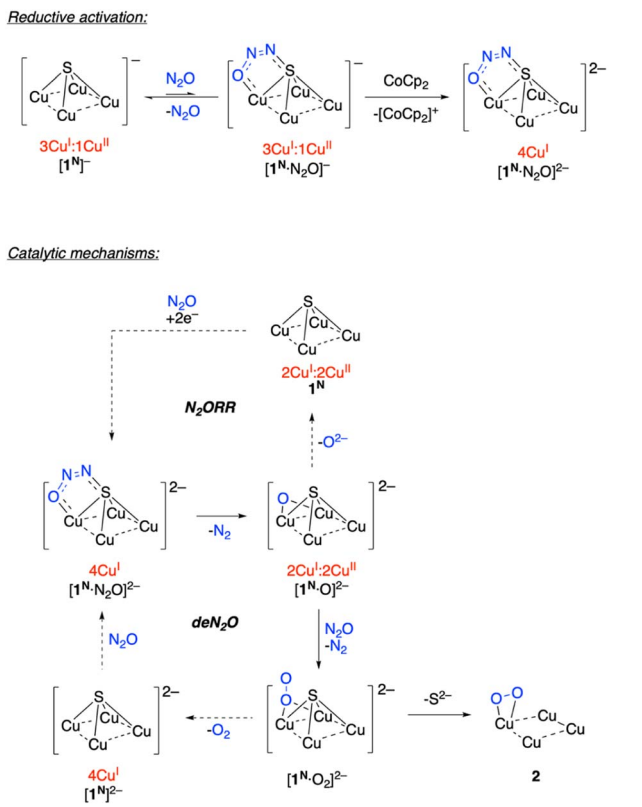

Scheme 2 Plausible mechanisms for N_2ORR and deN$_2$O.

To gain further insight, the deN$_2$O cycle was modeled computationally. The reaction energy profile is shown in Fig. 4, which features models for the four key intermediates as well as the two transition states associated with N–O cleavage of N_2O. The computed intermediate $[\mathbf{1^N}\cdot N_2O]^{2-}$ (**A**) is isostructural to $[\mathbf{1^C}\cdot N_2O]^{2-}$ calculated previously,[24] with μ-1,3-N_2O binding across a Cu–S edge of the cluster and significant N_2O activation according to the bent O–N–N angle of 126°. Loss of N_2 from **A** to form $[\mathbf{1^N}\cdot O]^{2-}$ (**B**) is exergonic by $\Delta G = -28.2$ kcal mol^{-1} and proceeds *via* transition state **TS1** with a barrier height of $\Delta G^{\ddagger} = 12.9$ kcal mol^{-1}. The structure of **TS1** differs from that of reactant **A** in that the N_2O ligand occupies a μ-1,1-*O* binding mode spanning a Cu–Cu cluster edge in **TS1**. This binding mode has been previously proposed for a synthetic model complex[34] and for N_2O activation by Cu-ZSM-5 [35] but differs from that proposed for Cu_Z itself.[12] At **TS1**, the N_2O molecule has undergone further activation as evidenced by the elongated N–O bond distance (1.57 Å) and contracted N–N bond distance (1.14 Å) relative to those in **A** (1.297 and 1.233 Å, respectively). The Cu–Cu edge of the cluster with the N_2O bound is short (2.54 Å) to accommodate the bridging ligand and is compensated by a long Cu–Cu distance of 3.35 Å along the edge opposite the N_2O ligand. The structure of **B** following N_2 loss features a μ-oxo ligand with a Cu–O–Cu angle of 87° and a Cu–Cu distance (2.56 Å) similar to that in **TS1**.

Oxygenation of **B** by N_2O to form $[\mathbf{1^N}\cdot O_2]^{2-}$ (**C**) was calculated to be exergonic by $\Delta G = -9.6$ kcal mol^{-1} and proceeds *via* transition state **TS2**. The structure of **TS2** features the N_2O substrate approaching the Cu–O–Cu unit with an O$\cdots$O distance of 1.84 Å. The N_2O unit is significantly activated in **TS2**, with a bent O–N–N angle of 143°, a long O–N distance of 1.50 Å, and a short N–N distance of 1.13 Å. Unlike compound **2** formed from S^{2-} loss, the structure of **C** features a μ_2:η^1-O_2 ligand. The calculated O–O distance of 1.35 Å in **C** is indicative of significant O_2 reduction,[31] though the Cu–O distances in **C** (2.02 and 2.06 Å) are longer than those calculated for **2**.

Loss of O_2 from **C** to form $[\mathbf{1^N}]^{2-}$ (**D**) was calculated to be exergonic by $\Delta G = -29.8$ kcal mol^{-1}. Unlike intermediates **B** and **C** and transition states **TS1** and **TS2** that all involve bridging *O*-ligands along one cluster edge, the structure of **D** features a nearly square-shaped tetracopper core, with all calculated Cu–Cu distances between 2.66 and 2.78 Å. To complete the hypothetical catalytic deN$_2$O cycle, coordination of N_2O to **D** to regenerate **A** was calculated to be endergonic by $\Delta G = +25.2$ kcal mol^{-1}. Thus, although the net deN$_2$O reaction is calculated to be favorable ($\Delta G_{rxn} = -42.4$ kcal mol^{-1}), the rate-

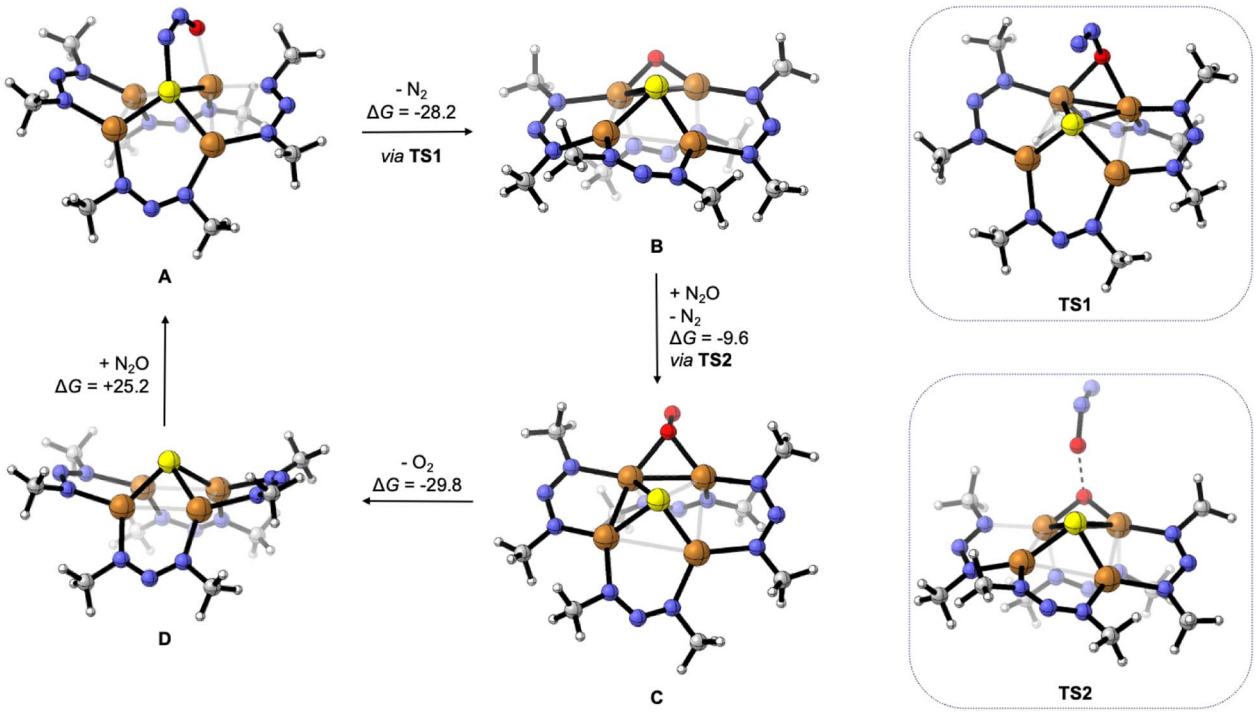

Fig. 4 Reaction intermediates and transition states for deN_2O calculated by DFT, with Gibbs free energy values given in units of kcal mol^{-1}. Computations were done at the B3LYP/def2TZVPP level of DFT using the CPCM implicit solvation model (CH_2Cl_2) except for **TS2** (see ESI†).

determining N_2O binding step prevents efficient catalysis under the experimental conditions examined, allowing for off-cycle conversion of **C** to inactive **2**. At this time, the path from **C** to **2** is ambiguous: it could involve simple S^{2-} dissociation from **C** to form **2** directly but could also involve exergonic O_2 dissociation from **C** to form **D** followed by O_2-promoted conversion of **D** to **2**.

Oxygenation of **B** to form **C** presumably involves nucleophilic addition of the N_2O oxygen to the electrophilic μ-oxo ligand of **B** (see **TS2**). In accord with that hypothesis, analysis of the frontier molecular orbitals of **B** indicated that the LUMO has significant (24%) oxygen 2p character (Fig. 5). One reason that the $\mathbf{1}^{\mathbf{N}}$ system is more likely than $\mathbf{1}^{\mathbf{C}}$ to do deN_2O chemistry might be the stabilization of this LUMO due to the electronegative nature of the NNN^- ligands relative to less electronegative NCN^-, thus favoring O–O coupling by N_2O nucleophilic addition in the NNN^- case. A second contributing reason could be that the relatively electron-withdrawing NNN^- ligands make the tetracopper core more Lewis acidic than for the NCN^- analogues, thus causing O^{2-} loss required for N_2ORR to be less facile for **B** and instead shunting the $\mathbf{1}^{\mathbf{N}}$ system into the deN_2O pathway.

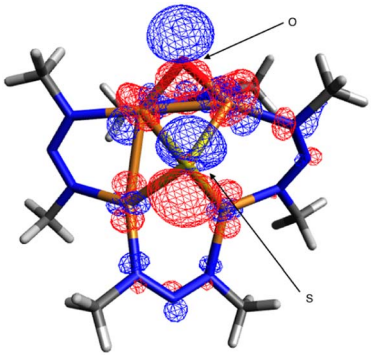

Fig. 5 Lowest unoccupied molecular orbital (0.03 isosurface) calculated for $[\mathbf{1}^{\mathbf{N}}\cdot O]^{2-}$ (**B**) by DFT at the B3LYP/def2TZVPP level using the CPCM implicit solvation model (CH_2Cl_2).

Conclusions

A redox pair of $Cu_4(\mu_4\text{-}S)$ clusters supported by triazenide ligands was synthesized and thoroughly characterized. While much of the characterization data mirrored those of the related formamidinate-supported system studied previously,[21–24] divergent reactivity behavior with N_2O was observed. While the formamidinate-ligated system was found to promote single-turnover N_2ORR akin to the biological Cu_Z cluster it mimics, the triazenide system was found to promote (inefficient) deN_2O reactivity that is a typical hallmark of heterogeneous catalysts like CuO/CeO_2. Computational modeling of the deN_2O pathway allowed for comparisons to be made with previously studied N_2ORR chemistry, enabling deeper understanding of factors influencing selectivity. A simple working model is as follows. The formamidinate system is relatively electron-rich, providing a "soft" tetracopper core that behaves like Cu_Z (that features a soft sulfide ligand) by readily dissociating O^{2-} upon N_2O deoxygenation to favor N_2ORR. On the other hand, the triazenide system is relatively electron-poor, providing a "hard" tetracopper core that behaves like CuO/CeO_2 (that features hard

oxide ligation) by forming a tightly-bound and electrophilic μ-oxo intermediate upon N_2O deoxygenation to favor deN_2O. These insights stand to inform future N_2O-fixing catalyst designs.

Data availability

Spectral data is reproduced in ESI,† and raw data are available from the author upon request. Computational output coordinates have been uploaded as ESI.† X-ray crystallography data is available upon request from the CCDC under deposition numbers 2299540 and 2299541.

Author contributions

N. P. M. carried out experiments, conducted computational modeling, and wrote the manuscript.

Conflicts of interest

There are no conflicts to declare.

Acknowledgements

Funding was provided by NIH/NIGMS under grant R35 GM140850. Computational resources and services were provided by the Advanced Cyberinfrastructure for Education and Research (ACER) group at UIC. Dr Daniel McElheny (UIC) and Dr Samantha MacMillan (Cornell) assisted with collection of EPR and X-ray diffraction data, respectively.

Notes and references

1 J. Hansen and M. Sato, *Proc. Natl. Acad. Sci. U. S. A.*, 2004, **101**, 16109–16114.
2 A. R. Ravishankara, J. S. Daniel and R. W. Portmann, *Science*, 2009, **326**, 123–125.
3 H. Tian, R. Xu, J. G. Canadell, R. L. Thompson, W. Winiwarter, P. Suntharalingam, E. A. Davidson, P. Ciais, R. B. Jackson, G. Janssens-Maenhout, M. J. Prather, P. Regnier, N. Pan, S. Pan, G. P. Peters, H. Shi, F. N. Tubiello, S. Zaehle, F. Zhou, A. Arneth, G. Battaglia, S. Berthet, L. Bopp, A. F. Bouwman, E. T. Buitenhuis, J. Chang, M. P. Chipperfield, S. R. S. Dangal, E. Dlugokencky, J. W. Elkins, B. D. Eyre, B. Fu, B. Hall, A. Ito, F. Joos, P. B. Krummel, A. Landolfi, G. G. Laruelle, R. Lauerwald, W. Li, S. Lienert, T. Maavara, M. MacLeod, D. B. Millet, S. Olin, P. K. Patra, R. G. Prinn, P. A. Raymond, D. J. Ruiz, G. R. van der Werf, N. Vuichard, J. Wang, R. F. Weiss, K. C. Wells, C. Wilson, J. Yang and Y. Yao, *Nature*, 2020, **586**, 248–256.
4 S. R. Pauleta, M. S. P. Carepo and I. Moura, *Coord. Chem. Rev.*, 2019, **387**, 436–449.
5 W. C. Trogler, *Coord. Chem. Rev.*, 1999, **187**, 303–327.
6 N. Lehnert, B. W. Musselman and L. C. Seefeldt, *Chem. Soc. Rev.*, 2021, **50**, 3640–3646.
7 C. Ferousi, S. H. Majer, I. M. Dimucci and K. M. Lancaster, *Chem. Rev.*, 2020, **120**, 5252–5307.
8 S. R. Pauleta, S. Dell'Acqua and I. Moura, *Coord. Chem. Rev.*, 2013, **257**, 332–349.
9 S. R. Pauleta, C. Carreira and I. Moura, in *Metalloenzymes in Denitrification: Applications and Environmental Impacts*, ed. I. Moura, L. B. Maia, S. R. Pauleta and J. J. G. Moura, Royal Society of Chemistry, 2017, pp. 141–169.
10 C. Carreira, S. R. Pauleta and I. Moura, *J. Inorg. Biochem.*, 2017, **177**, 423–434.
11 S. C. Rathnayaka and N. P. Mankad, *Coord. Chem. Rev.*, 2021, **429**, 213718.
12 E. M. Johnston, C. Carreira, S. Dell'Acqua, S. G. Dey, S. R. Pauleta, I. Moura and E. I. Solomon, *J. Am. Chem. Soc.*, 2017, **139**, 4462–4476.
13 E. M. Johnston, S. Dell'Acqua, S. Ramos, S. R. Pauleta, I. Moura and E. I. Solomon, *J. Am. Chem. Soc.*, 2014, **136**, 614–617.
14 A. Pomowski, W. G. Zumft, P. M. H. Kroneck and O. Einsle, *Nature*, 2011, **477**, 234–237.
15 A. Wüst, L. Schneider, A. Pomowski, W. G. Zumft, P. M. H. Kroneck and O. Einsle, *Biol. Chem.*, 2012, **393**, 1067–1077.
16 M. Konsolakis, *ACS Catal.*, 2015, **5**, 6397–6421.
17 M. H. Groothaert, K. Lievens, H. Leeman, B. M. Weckhuysen and R. A. Schoonheydt, *J. Catal.*, 2003, **220**, 500–512.
18 P. J. Smeets, M. H. Groothaert, R. M. van Teeffelen, H. Leeman, E. J. M. Hensen and R. A. Schoonheydt, *J. Catal.*, 2007, **245**, 358–368.
19 M. Zabilskiy, P. Djinović, B. Erjavec, G. Dražić and A. Pintar, *Appl. Catal., B*, 2015, **163**, 113–122.
20 B. J. Johnson, S. V. Lindeman and N. P. Mankad, *Inorg. Chem.*, 2014, **53**, 10611–10619.
21 S. C. Rathnayaka, C. W. Hsu, B. J. Johnson, S. J. Iniguez and N. P. Mankad, *Inorg. Chem.*, 2020, **59**, 6496–6507.
22 B. J. Johnson, W. E. Antholine, S. V. Lindeman and N. P. Mankad, *Chem. Commun.*, 2015, **51**, 11860–11863.
23 B. J. Johnson, W. E. Antholine, S. V. Lindeman, M. J. Graham and N. P. Mankad, *J. Am. Chem. Soc.*, 2016, **138**, 13107–13110.
24 S. C. Rathnayaka, S. M. Islam, I. M. Dimucci, S. N. MacMillan, K. M. Lancaster and N. P. Mankad, *Chem. Sci.*, 2020, **11**, 3441–3447.
25 C.-W. W. Hsu, S. C. Rathnayaka, S. M. Islam, S. N. MacMillan and N. P. Mankad, *Angew. Chem., Int. Ed.*, 2020, **59**, 627–631.
26 P. Alayoglu, T. Chang, M. V. Lorenzo Ocampo, L. J. Murray, Y.-S. Chen and N. P. Mankad, *Inorg. Chem.*, 2023, **62**, 15267–15276.
27 N. G. Connelly and W. E. Geiger, *Chem. Rev.*, 1996, **96**, 877–910.
28 K. Fujisawa, M. Tanaka, Y. Moro-oka and N. Kitajima, *J. Am. Chem. Soc.*, 1994, **116**, 12079–12080.
29 D. J. E. Spencer, N. W. Aboelella, A. M. Reynolds, P. L. Holland and W. B. Tolman, *J. Am. Chem. Soc.*, 2002, **124**, 2108–2109.
30 N. W. Aboelella, S. V. Kryatov, B. F. Gherman, W. W. Brennessel, V. G. Young, R. Sarangi, E. V. Rybak-

Akimova, K. O. Hodgson, B. Hedman, E. I. Solomon, C. J. Cramer and W. B. Tolman, *J. Am. Chem. Soc.*, 2004, **126**, 16896–16911.

31 D. A. Iovan, A. T. Wrobel, A. A. McClelland, A. B. Scharf, G. A. Edouard and T. A. Betley, *Chem. Commun.*, 2017, **53**, 10306–10309.

32 N. C. Tomson, K. D. Williams, X. Dai, S. Sproules, S. DeBeer, T. H. Warren and K. Wieghardt, *Chem. Sci.*, 2015, **6**, 2474–2487.

33 S. Ghosh, S. I. Gorelsky, P. Chen, I. Cabrito, J. J. G. Moura, I. Moura and E. I. Solomon, *J. Am. Chem. Soc.*, 2003, **125**, 15708–15709.

34 I. Bar-Nahum, A. K. Gupta, S. M. Huber, M. Z. Ertem, C. J. Cramer and W. B. Tolman, *J. Am. Chem. Soc.*, 2009, **131**, 2812–2814.

35 M.-L. L. Tsai, R. G. Hadt, P. Vanelderen, B. F. Sels, R. A. Schoonheydt and E. I. Solomon, *J. Am. Chem. Soc.*, 2014, **136**, 3522–3529.